RSC Advances

PAPER

View Article Online
View Journal | View Issue

Check for updates

Cite this: *RSC Adv.*, 2026, **16**, 19206

Received 2nd March 2026
Accepted 6th April 2026

DOI: 10.1039/d6ra01786j

rsc.li/rsc-advances

# High-performance $Ag_{0.333}V_2O_5$ nanowires as cathode materials for aqueous zinc-ion batteries

Yimeng Xu, *[ac] Junyu Qu,[ab] Xunna Ke,[ab] Hongrui Jiang[ab] and Ali Bahadur*[ab]

Aqueous zinc-ion batteries (AZIBs) have attracted wide attention for large-scale energy storage owing to their low cost and intrinsic safety. However, the development of high-performance cathode materials remains a challenge. Herein, a nanowire-like $Ag_{0.333}V_2O_5$ was synthesized *via* a facile one-step hydrothermal method and systematically investigated as a cathode material for AZIBs. Benefiting from its one-dimensional nanowire architecture and $Ag^+$ pre-intercalation, the as-prepared $Ag_{0.333}V_2O_5$ nanowires exhibit favorable electrochemical performance. They deliver a high specific capacity of 378 mAh $g^{-1}$ at a current density of 0.1 A $g^{-1}$, and an excellent cycling stability, retaining 92% of the initial capacity after 500 cycles at 2 A $g^{-1}$. These results demonstrate that the $Ag_{0.333}V_2O_5$ nanowires are promising cathode candidates for aqueous zinc-ion energy storage systems.

## Introduction

Rechargeable aqueous zinc-ion batteries (AZIBs) have recently emerged as a compelling alternative to lithium-ion batteries owing to their intrinsic safety, high theoretical capacity, low redox potential, and cost-effectiveness.[1,2] The use of aqueous electrolytes further improves operational safety and environmental sustainability, rendering AZIBs highly promising for large-scale energy storage applications. However, the practical implementation of AZIBs is still severely constrained by the lack of high-performance cathode materials that enable rapid and reversible $Zn^{2+}$ (de)intercalation without significant structural collapse during prolonged cycling.[3,4]

To date, various cathode materials have been explored for AZIBs, including manganese-based oxides, vanadium-based compounds, Prussian blue analogues, and organic frameworks.[5–10] Among these candidates, vanadium-based materials have attracted particular attention due to their multiple accessible oxidation states ($V^{3+}/V^{4+}/V^{5+}$), diverse crystallographic structures, and high theoretical capacities, which enable multielectron redox reactions and flexible $Zn^{2+}$ storage.[11] Nevertheless, most vanadium-based cathodes suffer from poor electronic conductivity, sluggish $Zn^{2+}$ diffusion kinetics, and structural instability during cycling.[12,13] These issues arise primarily from strong electrostatic interactions between divalent $Zn^{2+}$ ions and the host lattice, which induce lattice distortion, promote vanadium dissolution, and lead to capacity fading. To address these challenges, several modification strategies have been proposed: foreign-ion pre-intercalation to enlarge the interlayer spacing, nanostructure engineering to shorten the ion diffusion pathway, composites with conductive materials to increase electrical conductivity, and electrostatic screening to reduce the intercalation energy.[14,15] In particular, numerous studies have verified that pre-intercalation of metal ions (*e.g.*, $Na^+$, $K^+$, $Ca^{2+}$, and $Al^{3+}$) is effective in enlarging the interlayer spacing, stabilizing the host framework, and facilitating $Zn^{2+}$ transport.[16,17] For instance, CaVO nanoribbons synthesized by Niiu *et al.* delivered an initial discharge capacity of 300 mAh $g^{-1}$ at 0.1 A $g^{-1}$,[18] while $Co^{2+}$-substituted $VO_2$ reported by Zhang *et al.* exhibited suppressed vanadium dissolution and enhanced electronic conductivity and zinc ion mobility.[19] He Lin *et al.* reported $Al_{0.34}V_5O_{12}\cdot 2.4H_2O$ nanoribbons *via* the hydrothermal introduction of $Al^{3+}$, which demonstrate excellent electrochemical performance of 407.8 mAh $g^{-1}$ at 0.2 A $g^{-1}$.[20] In parallel, Wang *et al.* design a hierarchical nanoflowers structure of Zn-vanadium oxide material, which provides abundant contact between electrode and electrolyte that facilitates fast electrochemical kinetics. As a result, the battery delivered a high specific capacity of 426 mAh $g^{-1}$ at 0.1 A $g^{-1}$.[21]

Silver vanadium oxides (SVOs) are essential functional inorganic materials that have found applications in various electrochemical storage devices. $Ag_{0.33}V_2O_5$ has been reported as a promising cathode material with high capacity and stability for lithium-ion, aqueous zinc-ion, and manganese batteries.[22–24] The pre-intercalation $Ag^+$ ion was reported to improve the ion diffusion rate, modulate the layered structure, and enhance structural stability.[25] However, a clear understanding of the electrochemical behavior of $Ag_{0.33}V_2O_5$ within aqueous multivalent-ion systems remains elusive, particularly regarding the reversibility of the Ag species and structural evolution during cycling. Lan *et al.*

---

[a] College of Science, Mathematics, and Technology, Wenzhou-Kean University, Wenzhou 325060, Zhejiang Province, China. E-mail: xuyimeng@wku.edu.cn; Abahadur@wku.edu.cn

[b] Dorothy and George Hennings College of Science, Mathematics and Technology, Kean University, 1000 Morris Ave, Union NJ 07083, USA

[c] Wenzhou-Kean University Chemical Materials Research Center, China

attributed the outstanding performance of $Ag_{0.33}V_2O_5$ to enhanced conductivity of pre-intercalated $Ag^+$ and a vacancy-exchange mechanism of $Zn^{2+}/Ag^+$.[26] Guo *et al.* proposed that $Ag_{0.33}V_2O_5$ exhibits a high reversible combination displacement/intercalation mechanism: $Ag^0$ nanoparticles are generated upon $Zn^{2+}$ intercalation and are highly reversibly oxidized to $Ag^+$ upon $Zn^{2+}$ de-intercalation.[27] Wang *et al.* reported an *in situ* phase transformation to $Zn_3(OH)_2V_2O_7\cdot 2H_2O$, which will gradually replace the pristine material during cycling, accompanied by $Zn^{2+}/Ag^+$ exchange and metallic Ag formation.[28] These differing observations indicate that the $Zn^{2+}$ storage mechanism in $Ag_{0.33}V_2O_5$ remains under debate. Moreover, the strong electrostatic interaction between divalent $Zn^{2+}$ and the host lattice in vanadium oxides generally leads to sluggish diffusion kinetics, underscoring the need for structural regulation strategies,[29] and enhance structural stability. Thereby, making it challenging to achieve both fast kinetics and stable cycling performance in a single system.

In this work, we report a facile one-step hydrothermal synthesis of $Ag_{0.333}V_2O_5$ nanowires as a high-performance cathode material for aqueous zinc-ion batteries. The incorporation of $Ag^+$ pre-intercalation and a one-dimensional nanowire architecture are excepted to enhanced electronic conductivity, shorten $Zn^{2+}$ diffusion pathways, and mitigate structural strain during cycling. As a result, the $Ag_{0.333}V_2O_5$ nanowires deliver a high specific capacity of 378 mAh $g^{-1}$ at 0.1 A $g^{-1}$, and excellent cycling stability with 90% capacity retention after 500 cycles at 2 A $g^{-1}$.

## Experimental

### Synthesis of $Ag_{0.333}V_2O_5$ nanowires

The $Ag_{0.333}V_2O_5$ nanowires were synthesized *via* a one-step hydrothermal method with tartaric acid employed as a mild reducing agent. Typically, 0.468 g of $NH_4VO_3$ and 0.3 g of tartaric acid were dissolved in 100 mL of distilled water while stirring at 50 °C. Next, 3.5 mL of 3 M of $HNO_3$ solution was added dropwise to adjust the pH of the suspension until a clear, blue solution formed. After that, 0.1698 g of $AgNO_3$ was added with further stirring. The pH value of the final solution is approximately 2.5. The resulting homogeneous solution was transferred into a 150 mL Teflon-lined autoclave and heated at 180 °C for 24 h in a dry oven. After naturally cooling to room temperature, the precipitate was collected by filtration, rinsed with ethanol and water, and dried in a vacuum oven at 80 °C for 12 h.

### Characterization

The prepared samples were characterized using an X-ray diffractometer (XRD, Rigaku Ultima IV) with Cu Kα radiation. The elemental composition of the sample was analyzed by X-ray photoelectron spectroscopy (XPS; Thermo Scientific ESCALAB 250Xi). The morphology, structure, and size were obtained by scanning electron microscopy (SEM, Hitachi SU8010) and scanning transmission electron microscopy (STEM, FEI Talos F200S G2). The surface area was measured by nitrogen adsorption using the Brunauer–Emmett–Teller (BET) method on a Quantachrome Nova analyzer at 77 K.

### Electrochemical measurements

The electrochemical performance of the as-prepared $Ag_{0.333}V_2O_5$ as ZIBs cathode material was tested in an assembled 2032-type coin half-cell. The working electrode was fabricated by coating a slurry composed of 70 wt% active material, 20 wt% Super P conducting additive, and 10 wt% polyvinylidene fluoride (PVDF) binder in *N*-methyl-2-pyrrolidine (NMP) onto a titanium foil. The zinc foil was used as the counter electrode, and a Whatman GF/A glass fiber filter served as the separator. 3 M $Zn(CF_3SO_3)_2$ aqueous solution was employed as the electrolyte. The mass loading of active material ranges 2.2 to 2.8 mg per electrode, corresponding to an areal mass loading of approximately 1.95–2.48 mg $cm^{-2}$ on a circular titanium foil.

Galvanostatic charge and discharge tests and Galvanostatic Intermittent Titration Technique (GITT) experiments on the testing system (LAND CT2001A, Wuhan, China) over a voltage window of 0.2–1.6 V *vs.* $Zn/Zn^{2+}$ at various current densities. Cyclic voltammetry (CV) between 0.2 and 1.6 V at different scan rates was performed on the electrochemical workstation (CHI660E, Shanghai Chenhua Co., Ltd, China).

## Results and discussion

Various Ag/V precursor ratios was systematically explored, and the target phase was successfully obtained at an Ag/V ratio of 1 : 4 (Fig. S1). The crystal structure of the as-prepared sample was investigated by X-ray diffraction (XRD). As shown in Fig. 1a, all diffraction peaks can be well indexed to the standard diffraction peaks of monoclinic $Ag_{0.333}V_2O_5$ (PDF No. 81-1740),[30] confirming the formation of the target phase. The main peaks at 12.32, 18.72, 23.26, 26.42, 27.92, 29.32, 30.68, and 32.92° are assigned to the (200), (002), $(\bar{4}01)$, $(\bar{1}11)$, (111), (401), $(\bar{4}03)$ and $(\bar{3}12)$ crystal planes, respectively. No impurity phase was detected, indicating the high purity of the synthesized $Ag_{0.333}V_2O_5$.

X-ray photoelectron spectroscopy (XPS) was performed to elucidate the chemical states of the constituent elements (Fig. 1b–e). The Ag 3d XPS spectrum exhibits two characteristic peaks located at binding energies of 367.5 eV and 373.5 eV, assignable to Ag $3d_{5/2}$ and Ag $3d_{3/2}$ of monovalent $Ag^+$ species rather than metallic $Ag^0$. In the V 2p spectrum, peaks located at 524.2 eV and 516.9 eV correspond to the V $2p_{1/2}$ and V $2p_{3/2}$, respectively. The V 2p spectrum can be deconvoluted into contirbutions from $V^{5+}$ and $V^{4+}$ peaks within both regions, suggesting the coexistence of mixed valence states. The presence of $V^{4+}$ is attributed to a reduction of $V_2O_5$ during synthesis, while the introduction of $Ag^+$ serves as a charge-compensating species to maintain overall electroneutrality.[28] The O 1s spectrum in Fig. 1e can be fitted into two components located at 529.6 eV and 530.6 eV, corresponding to M=O and O-defects.[20] Oxygen vacancies were reported to provide additional active sites, enhance the conductivity, and promote the intercalation pseudocapacitive behavior.[31] Collectively, XRD and XPS results confirm the successful synthesis of phase-pure $Ag_{0.333}V_2O_5$ with the intercalation of $Ag^+$ into the vanadium structure.

Scanning electron microscopy (SEM) and transmission electron microscopy (TEM) are utilized to observe the

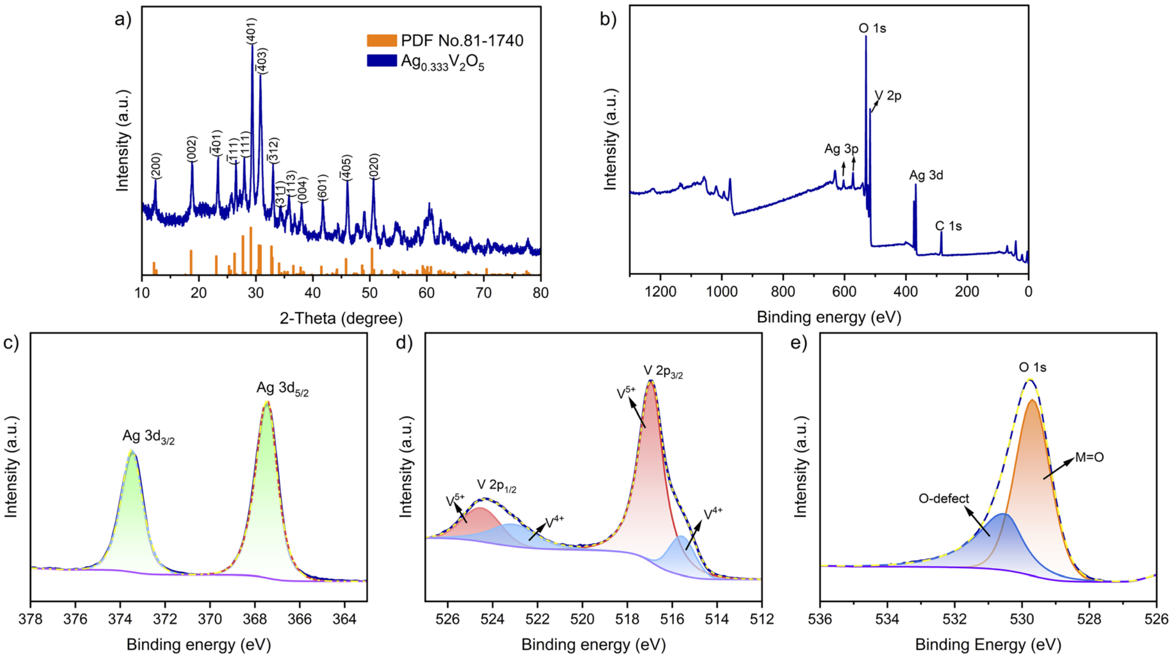

Fig. 1 Structural characterizations of the samples. (a) XRD pattern. (b) XPS survey spectrum. (c) Ag 3d. (d) V 2p. (e) O 1s.

morphologies of the as-prepared samples. Fig. 2a, b and c (SEM) and (TEM) images reveal an intertwined and uniform nanowire morphology. The individual nanowire exhibits an average diameter of approximately 50 nm, forming a well-connected network. Form the elemental mapping analysis (Fig. S2), the atomic ratio of Ag to V is determined to be approximately 1 : 6, which is consistent with the stoichiometry of $Ag_{0.333}V_2O_5$, further supporting the successful formation of the target phase. High-resolution TEM (HRTEM) image (Fig. 2d) exhibits clear lattice fringes with an interplanar spacing of 3.38 Å, which can be indexed to the ($\bar{1}$11) crystal plane of monoclinic $Ag_{0.333}V_2O_5$, indicative of high crystallinity of the nanowires. Furthermore, high-angle annular dark-field scanning TEM (HAADF-STEM) elemental mapping images (Fig. 2e–h) demonstrate a homogeneous distribution of Ag, V, and O throughout the nanowires, confirming the compositional uniformity of the material. The specific surface area was evaluated by nitrogen adsorption using the Brunauer–Emmett–Teller (BET) method. The surface area of the sample is 32.5 $m^2\ g^{-1}$, which is expected to provide sufficient electrode–electrolyte interface.

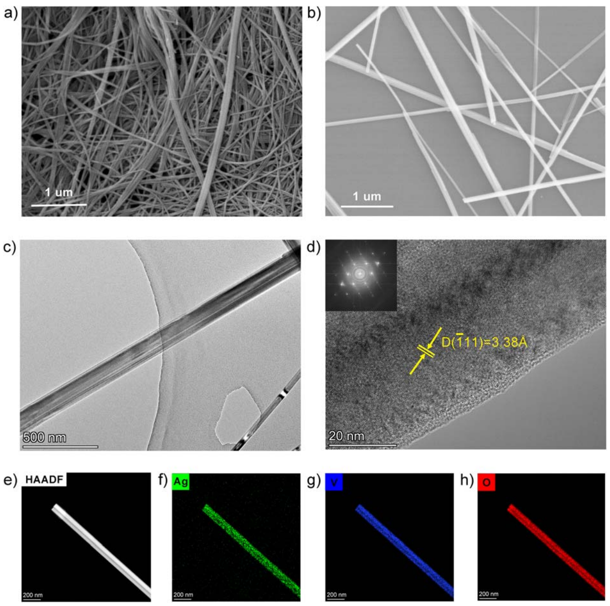

Fig. 2 (a and b) SEM images. (c and d) HRTEM images. (e–h) HAADF-STEM element mapping images.

Comprehensive structure characterization confirms the successful formation of phase-pure $Ag_{0.333}V_2O_5$. The interconnected one-dimensional nanowire is expected to shorten the $Zn^{2+}$ diffusion pathway. Thus, the synergistic effects of $Ag^+$ intercalation, oxygen defects and nanowires architecture are anticipated to enhance electronic conductivity, accelerated $Zn^{2+}$ transport kinetics, and deliver a superior electrochemical performance, which will be further investigated in the following study.

The electrochemical properties of $Ag_{0.333}V_2O_5$ were assessed in CR2032-type coin cells using metallic zinc as the anode and 3 M aqueous $Zn(CF_3SO_3)_2$ solution as the electrolyte. Fig. 3a presents the cyclic voltammetry (CV) pattern within a voltage window of 0.2–1.6 V (*versus* $Zn/Zn^{2+}$) at a scan rate of 0.1 mV $s^{-1}$. A dominant reduction peak emerges at 0.58 V, accompanied by additional features at 0.39 V, 0.51 V, and 0.73 V, which can be attributed to stepwise $Zn^{2+}$ insertion into the host framework.[26] In the reverse scan, two oxidation peaks emerge at 1.1 V and 0.75 V, corresponding to the reversible de-intercalation of $Zn^{2+}$ ions from the host structure. It is notable that distinct differences between the first cycle and the subsequent cycles, which can be commonly observed in vanadium-based oxide

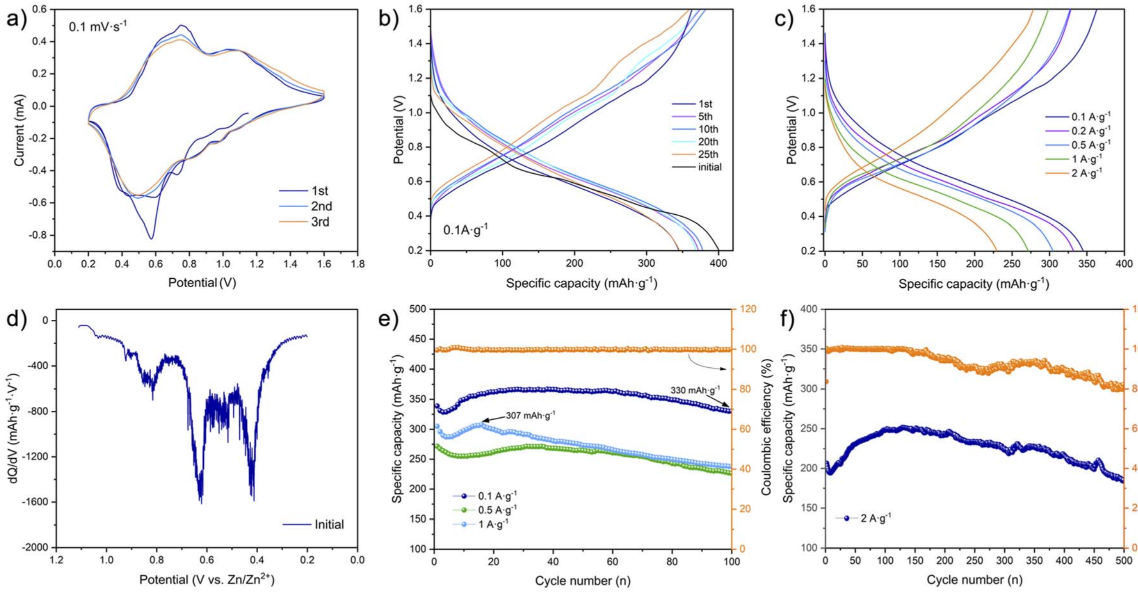

Fig. 3 (a) CV curves at 0.1 mV $s^{-1}$. (b) GCD curves of SVO at 0.1 A $g^{-1}$, (c) GCD curves of SVO at different current densities, (d) differential capacity ($dQ/dV$) curves of the initial discharge curve, (e) rate cycle performance, (f) long cycle performance of SVO at 2 A $g^{-1}$.

cathodes.[31] In our system, the presence of oxygen defects, as revealed by XPS analysis, suggests that vacancy filling and defect stabilization process. It is reported that oxygen vacancies may undergo migration or refilling during the initial cycles, which can lead to partially irreversible processes.[32] To gain deeper insight into the redox processes, differential capacity ($dQ/dV$) curves were derived from the initial galvanostatic charge–discharge (GCD) profile (Fig. 3d). Two apparent peaks are observed at approximately 0.43 and 0.62 V, indicating two discharge platforms during the ion intercalation process and further confirming the stepwise storage behavior of zinc ions.

Galvanostatic charge–discharge tests demonstrate the excellent electrochemical performance of the $Ag_{0.333}V_2O_5$ cathode. As shown in Fig. 3b, the electrode delivers a highest specific capacity of 378 mAh $g^{-1}$ at a current density of 0.1 A $g^{-1}$ and presents a good reversibility. The rate performance of the electrode at various current densityies is shown in Fig. 3c, e and S4. It demonstrates favourable rate capability with discharge capacities of 345, 332, 304, 271, and 230 mAh $g^{-1}$ at current densities of 0.1, 0.2, 0.5, 1, and 2 A $g^{-1}$, respectively. The electrode also exhibits stable cycling performance, retaining discharge capacities of 237 and 226 mAh $g^{-1}$ after 100 cycles at 0.5 and 1 A $g^{-1}$, respectively. A comparison of zinc-ion storage performance with previously reported cathode materials is summarized in Table 1.[33–41] The electrochemical performance in this work is highly competitive compared among silver vanadium oxide cathodes.

Notably, a gradual capacity increment is observed in the initial stages of cycling. The increment trend can be attributed to an activation process associated with improved the electrolyte penetration and enhanced utilization of active sites within the entangled nanowire structure.[42] For long-term cycling assessment, the $Ag_{0.333}V_2O_5$ cathode was tested at a current density of 2 A $g^{-1}$. As shown in Fig. 3f, it displays a high discharge specific capacity of 250 mAh $g^{-1}$ and retains 92% of its initial capacity after 500 cycles, demonstrating exceptional long-term cycling stability.

To further investigate the electrochemical kinetics of $Ag_{0.333}V_2O_5$, CV measurements were conducted at scan rates ranging from 0.1 to 0.5 mV $s^{-1}$. As shown in Fig. 4a, with increasing scan rate, the anodic peaks shift slightly toward higher potentials and the cathodic peaks move toward lower potentials, while the overall CV curves remain well preserved, suggesting low polarization and good reversibility. The kinetic behavior was analyzed based on the relationship between the peak current ($i$) and scan rate ($v$), expressed as:

$$i = av^b$$

where $a$ and $b$ are regulable values.[43] The $b$-value can be obtained from the slope of the linear fitting of $\log(i)$ *versus* $\log(v)$. In general, a $b$-value close to 1 indicates a surface-controlled process, whereas a $b$-value close to 0.5 corresponds to diffusion-limited behavior. As illustrated in Fig. 4b, the $b$-value of peaks 1–4 are calculated to be 0.804, 0.973, 0.893, and 0.843, respectively. All fitted values exhibit correlation coefficients ($R^2 > 0.99$), indicating excellent linearity and reliability of the fitting. The intermediate $b$-values reveal that $Zn^{2+}$ storage in $Ag_{0.333}V_2O_5$ follows a mixed mechanism, with a dominant contribution from surface-controlled processes.

Additionally, the relative contributions of capacitive and diffusion-controlled processer were quantitatively analysed *via* Dunn's method based on the equation:

$$i = k_1v + k_2v^{1/2}$$

where $k_1v$ represents the capacitive-controlled contribution and $k_2v^{1/2}$ corresponds to the diffusion-controlled contribution.[44,45] The capacitive contribution was obtained by integrating the $k_1v$ component over the entire potential window.

Table 1 The electrochemical performance of silver vanadium oxides electrodes reported for AZIBs

| Materials | Morphology | Discharge capacity (mAh $g^{-1}$/A $g^{-1}$) | Cycling stability (mAh $g^{-1}$/A $g^{-1}$/cycles) | Voltage window (V) | Ref. |
|---|---|---|---|---|---|
| $V_2O_5$ | Nanofibers | 265/0.02 | 116/0.588/500 | 0.5–1.5 | 33 |
| $V_2O_5$ | Nanowires | 317/0.2 | 97.4/2000/1 | 0.2–1.6 | 34 |
| $V_2O_5$ | Hollow spheres | 280/0.2 | 108/6200/10 | 0.2–1.6 | 35 |
| $Ag_{0.33}V_2O_5$ | Nanorods | ~150/0.5 | 70/3/700 | 0.2–1.6 | 26 |
| $Ag_{0.33}V_2O_5$ | Nanorods | ~210/0.5 | 144/2/500 | 0.1–1.6 | 25 |
| $Ag_{0.33}V_2O_5$ | Nanobelts | ~300/0.1 | 150/2/3000 | 0.4–1.4 | 28 |
| $Ag_2V_4O_{11}$ | Micro-rods | ~221/0.5 | 117/3/1000 | 0.3–1.3 | 36 |
| $Ag_{1.2}V_3O_8$ | Nanorods | ~150/1 | — | 0.4–1.4 | 27 |
| $Ag_{0.4}V_2O_5$ | Nanobelts | 237/0.5 | 216/5/1000 | 0.4–1.4 | 37 |
| $K_{0.23}V_2O_5$ | — | 284/0.1 | 103/2/500 | 0.1–1.7 | 38 |
| $Zn_xV_2O_5\cdot nH_2O$ | Flower-like | 324/0.1 | 200/5/2000 | 0–1.5 | 39 |
| $Na_{0.13}(NH_4)_{0.5}V_2O_5\cdot 5H_2O$ | Nanorod | 267/1 | 245/5/2000 | 0.4–1.6 | 40 |
| $Cu_{0.4}V_2O_5$ | Nanoflake | 358.3/0.1 | 128/2/1000 | 0.2–1.4 | 41 |
| $Ag_{0.333}V_2O_5$ | Nanowires | ~332/0.2 | 180/2/500 | 0.2–1.6 | This work |

As shown in Fig. 4c, the orange region represents the capacitive contribution, accounting for 80.9% at a scan rate of 0.3 mV $s^{-1}$. The capacitive contribution with scan rate increased from 0.1–0.5 mV $s^{-1}$ is summarized in Fig. 4d. The capacitive contributions are 78.9%, 79.0%, 80.9%, 85.0% and 89.9%, demonstrating in Fig. S3, confirming the predominance of fast surface-controlled kinetics, in good agreement with the *b*-value analysis discussed above. The high capacitive contributions can be partly attributed to the presence of oxygen defects which are considered to provide additional active sites and facilitate fast surface-controlled $Zn^{2+}$ storage.[31] Moreover, the interconnected nanowire network further promotes efficient charge transfer and ion transport, collectively contributing to enhanced pseudocapacitive behaviour.

The $Zn^{2+}$ diffusion kinetics were further examined by galvanostatic intermittent titration technique (GITT) measurements. The $Zn^{2+}$ diffusion coefficient ($D_{Zn}{}^{2+}$) was calculated based on the standard the equation:

$$D_{Zn^{2+}} = \frac{4}{\pi\tau}\left(\frac{m_B}{M_B}\frac{V_m}{S}\right)^2\left(\frac{\Delta E_s}{\Delta E_t}\right)^2$$

where $\tau$ is the pulse duration, $M_B$ and $V_M$ denote the molar mass and the molar mass of the material, $m_B$ is the mass of the active material, and $S$ is the electrode/electrolyte contact area.[20] $\Delta E_s$ and $\Delta E_t$ can be obtained from the GITT curves (Fig. 4f).

Typically, the coin cell was subjected to a constant current density of 0.1 A $g^{-1}$ for 600 s, followed by a shelved process for 1 h. The calculated zinc ion diffusion coefficients of SVO in Fig. 4g fall in the range of $10^{-11}$ to $10^{-10}$ $cm^2$ $s^{-1}$ throughout the charge–discharge process. These values are higher than those reported for pristine $V_2O_5$ cathodes ($10^{-12}$ to $10^{-11}$ $cm^2$ $s^{-1}$),[46] suggesting improved $Zn^{2+}$ transport kinetics in the present system. The enhancement is reasonably associated with $Ag^+$ pre-intercalation and one-dimensional nanowire architecture, which together may facilitate ion diffusion and charge transfer during repeated cycling.

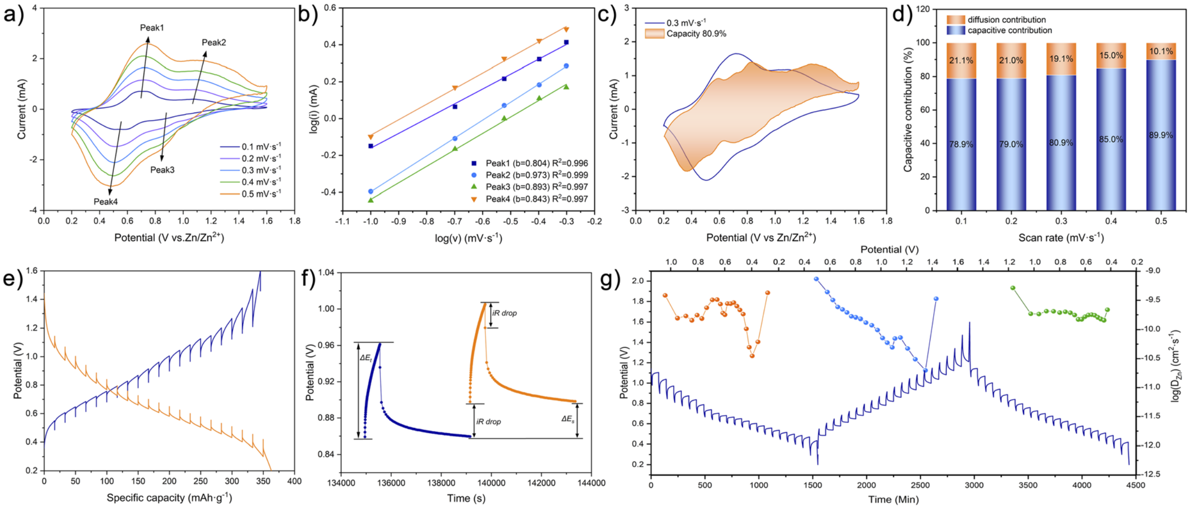

Fig. 4 (a) CV curves of the SVO at scan rates from 0.1 to 0.5 mV $s^{-1}$. (b) Fitting plots of log(*i*) *versus* log(*v*) at specific peak currents. (c) CV curve and calculated capacitive contribution at 0.3 mV $s^{-1}$. (d) Capacitive contribution ratios at various scan rates. (e–g) Discharge and charge GITT curves at 0.1 A $g^{-1}$ and corresponding $Zn^{2+}$ diffusion coefficient.

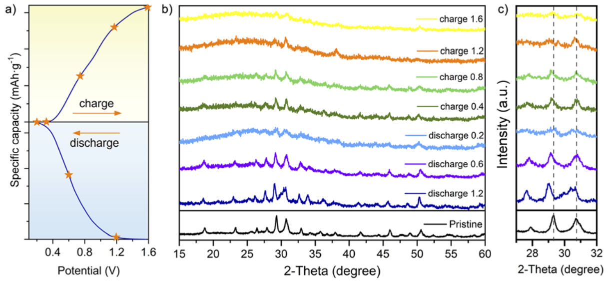

Fig. 5 (a) The second discharge–charge curves at 0.1 A $g^{-1}$. (b and c) *Ex situ* XRD patterns of the $Ag_{0.333}V_2O_5$ cathode at different states during the discharge–charge process.

*Ex situ* XRD measurements were carried out to monitor the structural evolution of $Ag_{0.333}V_2O_5$ during electrochemical cycling (Fig. 5a–c). Throughout the charge–discharge process, the characteristic diffraction peaks are well preserved, while a slight shift of the diffraction peak from 29.32° to 29.1° and peak broadening are observed, implying reversible interlayer expansion associated with ion insertion.[47] Such peak evolution is characteristic of lattice breathing in layered structures, where guest-ion insertion/extraction induces reversible lattice distortion without losing crystallinity.[48] Importantly, no new diffraction peaks emerge during cycling, excluding the formation of irreversible phases. Although the diffraction intensities decrease at the fully discharged and charged states, the characteristic reflections remain identifiable and recover at intermediate states. This behavior suggests that preserved structural integrity rather than framework collapse. Overall, the *ex situ* XRD results demonstrate that the $Ag_{0.333}V_2O_5$ framework maintains it structural integrity during repeated $Zn^{2+}$ insertion and extraction. The pre-intercalated $Ag^+$ ions is likely beneficial for stabilizing the V–O framework and enabling reversible lattice breathing, which is consistent with the excellent cycling electrochemical performance.

## Conclusions

In summary, one-dimensional $Ag_{0.333}V_2O_5$ nanowires were successfully synthesized *via* a facile one-step hydrothermal method and demonstrated effective $Zn^{2+}$ storage behavior in aqueous zinc-ion batteries. The enhanced electrochemical performance can be attributed to a synergistic effect of structure and electronic factors: (i) pre-intercalation $Ag^+$ help maintain the structure and improve electronic conductivity; (ii) the one-dimensional nanowire architecture shortens $Zn^{2+}$ diffusion pathways and enhances electrolyte accessibility. (iii) the presence of oxygen defects, as revealed by XPS analysis, provides abundant active sites and promotes surface-controlled charge storage. The synergistic effects enable fast $Zn^{2+}$ storage reaction kinetics, improved $Zn^{2+}$ ion diffusion, and robust structural stability. As a result, the $Ag_{0.333}V_2O_5$ cathode delivers a high specific capacity, excellent rate capability and long-term cycling stability. This work highlights the effectiveness of $Ag^+$ pillars in stabilizing vanadium-based frameworks and provides a generalizable design strategy for developing high-performance cathode materials for vanadium-based cathodes in aqueous zinc-ion batteries.

## Author contributions

Yimeng Xu: conceptualization, data curation, formal analysis, visualization and writing—original draft and review. Junyu Qu: material preparation and characterization. Xunna Ke and Hongrui Jiang: electrochemical performance inverstigation. Ali Bahadui: supervision and writing—review and editing.

## Conflicts of interest

There are no conflicts to declare.

## Data availability

The data supporting the finding of this study are available within the article and its accompanying supplementary information (SI). Supplementary information: additional XRD, Dunn analysis, SEM-EDS, and electrochemical data. See DOI: https://doi.org/10.1039/d6ra01786j.

## Acknowledgements

We thank Public Technology Service Center of the Wenzhou Institute. UCAS for instrument availability that supported this work. We are grateful for the financial support from the Zhejiang Provincial Education Department General Program (No. Y202147286), Wenzhou Science and Technology Program (No. GC20250037), and the International Collaborative Research Program (No. ICRP2023008).

## Notes and references

1 B. Tang, L. Shan, S. Liang and J. Zhou, *Energy Environ. Sci.*, 2019, **12**, 3288–3304.
2 H. Chen, W. Huang and Z. Deng, *Adv. Energy Mater.*, 2025, **15**, 2501052.
3 Y. Bai, Y. Qin, J. Hao, H. Zhang and C. M. Li, *Adv. Funct. Mater.*, 2024, **34**, 23010393.
4 T. Song, W. Fan, Y. Hu, H. Zhang and Y. Bai, *Green Chem.*, 2025, **27**, 10071–10092.
5 M. Song, H. Tan, D. Chao and H. J. Fan, *Adv. Funct. Mater.*, 2018, **28**, 1802564.
6 S. F. Jia, L. Li and Y. Shi, *Nanoscale*, 2024, **16**, 1539–1576.
7 T. Lv, Y. Peng, G. Zhang, S. Jiang, Z. Yang, S. Yang and H. Pang, *Adv. Sci.*, 2023, **10**, 2206907.
8 Y. Li, J. Zhao, Q. Hu, T. Hao, H. Cao, X. Huang, Y. Liu, Y. Zhang, D. Lin, Y. Tang and Y. Cai, *Mater. Today Energy*, 2022, **29**, 101095.
9 X. Xu, Y. Chen, D. Liu, D. Zheng, X. Dai, W. Shi and X. Cao, *Chem. Rec.*, 2022, **22**, e202200079.
10 Z. Li, J. Tan, Y. Wang, C. Gao, Y. Wang, M. Ye and J. Shen, *Energy Environ. Sci.*, 2023, **16**, 2398–2431.

11 S. Zhang, H. Tan, X. Rui and Y. Yu, *Acc. Chem. Res.*, 2020, **53**, 1660–1671.

12 X. Chen, H. Zhang, J.-H. Liu, Y. Gao, X. Cao, C. Zhan, Y. Wang, S. Wang, S.-L. Chou, S.-X. Dou and D. Cao, *Energy Storage Mater.*, 2022, **50**, 21–46.

13 T. Zhou and G. Gao, *J. Energy Storage*, 2024, **84**, 110808.

14 Y. Yuan, S. Wu, X. Song, J. Y. Lee and B. Kang, *Energy Environ. Mater.*, 2024, **7**, e12632.

15 Q. Zhu, Z. Wang, J. Wang, X. Liu, D. Yang, L. Cheng, M. Tang, Y. Qin and H. Wang, *Rare Met.*, 2021, **40**, 309–328.

16 C. Xia, J. Guo, P. Li, X. Zhang and H. N. Alshareef, *Angew. Chem., Int. Ed.*, 2018, **57**, 3943–3948.

17 Z. Hao, J. Wang, J. Feng, Y. Fan, J. Peng, J. Wang and S. Dou, *Carbon Energy*, 2025, **7**, e681.

18 Y. Zhang and F. Wang, *Nat. Commun.*, 2020, **11**, 1–9.

19 Y. Zhang, X. Liu, J. Wang, *et al.*, *Angew. Chem., Int. Ed.*, 2023, **62**, e202216089.

20 J. Xu, Y. Zhang, C. Liu, H. Cheng, X. Cai, D. Jia and H. Lin, *Small*, 2022, **18**, 2204180.

21 L. Wang, K. Huang, J. Chen and J. Zheng, *Sci. Adv.*, 2019, **5**, eaax4279.

22 L. Liang, Y. Xu, Y. Lei and H. Liu, *Nanoscale*, 2014, **6**, 3536–3543.

23 W. Hu, X. Zhang, Y. Cheng, C. Wu, F. Cao and L. Wang, *ChemSusChem*, 2011, **4**, 1091–1094.

24 H. Lee, H. Lee, J. Pyun, S. Hong and M. S. Chae, *Adv. Sci.*, 2024, **11**, 2406642.

25 Z. Su, R. Wang, J. Huang, R. Sun, Z. Qin, Y. Zhang and H. Fan, *Rare Met.*, 2022, **41**(8), 2844–2852.

26 B. Lan, Z. Peng, L. Chen, C. Tang, S. Dong, C. Chen, M. Zhou, Q. An and P. Luo, *J. Alloys Compd.*, 2019, **787**, 9–16.

27 S. Guo, G. Fang, S. Liang, M. Chen, X. Wu and J. Zhou, *Acta Mater.*, 2019, **180**, 51–59.

28 Z. Wang, J. Diao, K. Kawashima, J. A. Weeks, R. R. Vaidyula, R. A. Marquez, N. Miller, G. Henkelman and C. B. Mullins, *J. Mater. Chem. A*, 2023, **11**, 18881–18892.

29 X. Jia, C. Liu, Z. G. Neale, J. Yang and G. Cao, *Chem. Rev.*, 2020, **120**, 7795–7866.

30 S. Liang, Y. Yu, T. Chen, A. Pan, S. Zhang, J. Zhou, Y. Tang, X. Tan and X. Tan, *Mater. Lett.*, 2013, **109**, 92–95.

31 F. Liang, M. Chen, S. Zhang, Z. Zou, C. Ge, S. Jia, S. Le, F. Yu and J. Nong, *ACS Sustainable Chem. Eng.*, 2024, **12**, 5117–5128.

32 Y. Fang, C. Qi, W. Bao, F. Xu, W. Sun, B. Liu, X. Yu, L. Wang, W. Jiang, P. Qiu and W. Luo, *Energy Environ. Sci.*, 2025, **18**, 367.

33 X. Chen, L. Wang, H. Li, F. Cheng and J. Chen, *J. Energy Chem.*, 2019, **38**, 20–25.

34 F. Mao, Y. Li, Z. Zou, B. Huang, J. Yang and J. Yao, *Electrochim. Acta*, 2021, **397**, 139255.

35 H. Qin, L. Chen, L. Wang, X. Chen and Z. Yang, *Electrochim. Acta*, 2019, **306**, 307–316.

36 X. Tong, J. Zhong, X. Hu and F. Zhang, *Crystals*, 2023, **13**, 565.

37 L. Shan, Y. Yang, W. Zhang, H. Chen, G. Fang, J. Zhou and S. Liang, *Energy Storage Mater.*, 2019, **18**, 10–14.

38 W. Zhang, C. Tang, B. Lan, L. Chen, W. Tang, C. Zuo, S. Dong, Q. An and P. Luo, *J. Alloys Compd.*, 2020, **819**, 152971.

39 M. K. Singh, S. Aware, P. Jaiswal, S. Gupta, K. Singh, N. Chaudhary, G. K. Maurya and D. K. Rai, *Chem. Commun.*, 2025, **61**, 11838.

40 Z. Wang, H. Wang, X. Bai, J. Dong, K. Zhang, K. Zhan and B. Zhao, *ACS Appl. Nano Mater.*, 2024, **7**, 27090–27099.

41 H. Zeng, J. Huang, Y. Chen, L. Chen, Z. Wu, H. Yang and Z. Chen, *Tungsten*, 2025, **7**, 547–556.

42 Y. Xu, W. Shen, A. Zhang, H. Liu and Z. Ma, *J. Mater. Chem. A*, 2014, **2**, 12982–12989.

43 T. S. Mathis, N. Kurra, X. Wang, D. Pinto, P. Simon and Y. Gogotsi, *Adv. Energy Mater.*, 2019, **9**, 1902007.

44 M. Zhang, S. Li, X. Wu and A. Abdukader, *Mater. Adv.*, 2024, **5**, 3965.

45 H. Chen, N. Qiu, B. Wu, Z. Yang, S. Sun and Y. Wang, *RSC Adv.*, 2019, **9**, 28908–28915.

46 S. Li, X. Wei, C. Wu, B. Zhang, S. Wu and Z. Lin, *ACS Appl. Energy Mater.*, 2021, **4**, 4208–4216.

47 C. Xia, J. Guo, Y. Lei, H. Liang, C. zhao and H. N. Alshareef, *Adv. Mater.*, 2018, **30**, 1705580.

48 Q. Wei, Z. Jiang, S. Tan, Q. Li, L. Huang, M. Yan, L. Zhou, Q. An and L. Mai, *ACS Appl. Mater. Interfaces*, 2015, **7**, 18211–18217.